Nanoscale

PAPER

CrossMark
click for updates

Optimizing the electric field around solid and core–shell alloy nanostructures for near-field applications

Luis Montaño-Priede,[a] Ovidio Peña-Rodríguez,*[b] Antonio Rivera,[b] Andrés Guerrero-Martínez[c] and Umapada Pal*[a]

The near electric field enhancement around plasmonic nanoparticles (NPs) is very important for applications like surface enhanced spectroscopies, plasmonic dye-sensitized solar cells and plasmon-enhanced OLEDs, where the interactions occur close to the surface of the NPs. In this work we have calculated the near-field enhancement around solid and core–shell alloy NPs as a function of their geometrical parameters and composition. We have found that the field enhancement is lower in the Au_xAg_{1-x} alloys with respect to pure Ag NPs, but it is still high enough for most near-field applications. The higher order modes have a stronger influence over the near-field due to a sharper spatial decay of the near electric field with the increase of the order of multipolar modes. For the same reason, in $Au_xAg_{1-x}@SiO_2$ core–shell structures, the quadrupolar mode is dominant around the core, whereas the dipolar mode is predominant around the shell. The LSPR modes can have different behaviours in the near- and the far-field, particularly for larger particles with high Ag contents, which indicates that caution must be exercised for designing plasmonic nanostructures for near-field applications, as the variations of the LSPR in the near-field cannot be inferred from those observed in the far-field. These results have important implications for the application of gold–silver alloy NPs in surface enhanced spectroscopies and in the fabrication of plasmon-based optoelectronic devices, like dye-sensitized solar cells and plasmon-enhanced organic light-emitting diodes.

Introduction

Despite their use for several centuries,[1] noble metal nanoparticles (NPs) are being studied actively nowadays due to their interesting optical properties and promising technological applications. Optical properties of these structures are dominated by the localized surface plasmon resonance (LSPR), a phenomenon produced by the collective oscillation of conduction electrons in resonance with the incoming light. The frequency of the LSPR (ω_{LSPR}) is sensitive to various parameters, such as the size, shape, surrounding medium and composition of the NPs.[2] When a plasmonic NP is excited with radiation of frequency ω_{LSPR}, the electric field close to the NP is increased (near-field) and the light is absorbed and/or scattered (far-field).[3] This localized electric field enhancement is responsible for phenomena such as surface-enhanced Raman scattering

(SERS),[4,5] surface-enhanced fluorescence,[6–8] and/or plasmonic resonance energy transfer,[9] which can be used in applications such as chemical and biological sensing[10,11] and thermal treatment of cancer cells.[12]

Plasmonic NPs are also useful for improving the efficiency of solar cells[13,14] and other optoelectronic devices.[15,16] For some applications, such as in dye-sensitized solar cells (DSSCs), it is important to isolate the metal NPs with dielectric materials, like SiO_2 or TiO_2, to prevent corrosion[17] or the recombination of photogenerated charge carriers.[13] Dielectric coatings around plasmonic NPs introduce modifications in the near electric field,[18] modulating the position and intensity of the surface plasmon absorbance band.[19,20] These adjustable optical properties of metal@dielectric core–shell structures make them attractive for utilization as supporting matrices for fluorophores[21,22] and fabrication of tuneable luminescent devices.[23] However, one of the most attractive applications of plasmonic NPs is for improving light emission in organic light-emitting diodes (OLEDs). OLEDs are being considered as next-generation display devices due to their low-cost, mechanical flexibility, and amenability to large-area fabrication based on printing techniques.[24] Nearly 100% internal quantum efficiency has been achieved for these devices[25] but their external quantum efficiency (EQE) is severely

[a]Instituto de Física, Benemérita Universidad Autónoma de Puebla, Apdo. Postal J-48, Puebla, Puebla, 72570, Mexico. E-mail: upal@ifuap.buap.mx
[b]Instituto de Fusión Nuclear, Universidad Politécnica de Madrid, C/José Gutiérrez Abascal 2, E-28006 Madrid, Spain. E-mail: ovidio@bytesfall.com
[c]Departamento de Química Física I, Universidad Complutense de Madrid, Avda. Complutense s/n, E-28040 Madrid, Spain

damped by the poor light extraction.[26] Considerable improvements in light extraction have been reported using the LSPR of plasmonic NPs like silver[27,28] and gold.[29]

Gold and silver have distinct plasmonic properties: the latter has a stronger and narrower absorption band than the former, but it is prone to oxidation, even at room temperature (RT), whereas gold is chemically stable at RT. Au_xAg_{1-x} alloys are an interesting option to overcome this problem because they can combine the best of both metals: an intense LSPR with a good chemical stability. Therefore, recent research interest has turned to the fabrication of gold–silver alloy NPs for applications in sensing,[30] SERS,[31] photocatalysis,[32–35] and DSSCs.[36] For application in OLEDs, nanoparticles of Au–Ag alloys might prove advantageous over their monometallic counterparts, as their LSPR can be tuned across a large region of the visible spectrum, which has not yet been explored.

Finally, it should be noted that the light emission gains produced by the introduction of plasmonic nanostructures is not assured because there are two competing processes: (i) the spontaneous emission enhancement due to the coupling between the LSPR and the excitons in the emitting layer and (ii) the exciton quenching and light absorption by the plasmonic structures. Therefore, the environment in which noble metal nanostructures are incorporated with emissive molecules in OLEDs should be optimized to maximize the radiative enhancement by coupling between excitons and surface plasmons.[28] Metal@dielectric core–shell nanostructures are an easy and effective way of enhancing the EQE by controlling the distance between the luminescent molecule and the plasmonic NP. Before the use of plasmonic alloy nanostructures for this purpose becomes a reality, theoretical simulations are required to develop an in-depth understanding of the linear optical properties of alloy and core@shell type plasmonic nanostructures. Likewise, it is necessary to understand the dependence of the near-field enhancements on the geometrical parameters of the nanostructures and the relationship between the near- and far-field spectra. Only then will it be possible to design and fabricate NPs suitable for SERS, DSSCs, OLEDs and other optoelectronic applications.

Calculation of the near-field enhancements is relatively easy for core–shell nanostructures[37] but unavailability of reliable optical datasets has greatly limited these simulations for Au_xAg_{1-x} alloys because they either do not reproduce the experimental results well or their validity is dubious in some cases. However, the optical constants for Au_xAg_{1-x} alloys have been systematically determined recently[38] for various compositions, which can be used to simulate the optical properties of alloy NPs, reproducing accurately the existing experimental results. In this work we have calculated the near electric field around solid (Au_xAg_{1-x}) and core–shell ($Au_xAg_{1-x}@SiO_2$) spherical NPs as a function of their composition (from $x = 0$ to $x = 1$), core radius (from 1 to 100 nm) and shell thickness (from 0 to 50 nm) using scattnlay 2.0,[39] a computer implementation based on Mie theory.[40] For all the samples, the fourth-power of the near electric field was calculated to evaluate their applicability as SERS substrates.[41]

Calculations and theoretical considerations

Near electric fields for solid and core–shell alloy NPs were calculated for an incident plane wave propagating along the z-direction and polarized in the x-direction, $\mathbf{E}_i = E_0 \exp[ikz\cos(\theta)]\hat{\mathbf{e}}_x$ (Fig. 1). The layer l can be defined by its size parameter $x_l = 2\pi n_m r_l/\lambda$ and a relative refractive index $m_l = n_l/n_m$, where λ is the wavelength of the incident wave in vacuum, r_l and n_l, $l = 1, 2, ..., L$, are the radius and complex refractive index of each layer, respectively. For the core–shell structures analysed in this work, we have used the indices c and s for the alloy core ($l = 1$) and the SiO_2 shell ($l = L = 2$, $n_s = 1.52$ (ref. 42)), respectively, and n_m is the refractive index of the surrounding medium (water, $n_m = 1.335$ (ref. 43)). Complex refractive indexes (n_c) of Au_xAg_{1-x} were taken from the work of Peña-Rodríguez et al.[38]

The electric field at any point can be expressed as the superposition of inward ($\mathbf{E}_{in}$) and outward ($\mathbf{E}_{out}$) sets of spherical wave functions. The electric fields, $\mathbf{E}_{in}$ and $\mathbf{E}_{out}$ can be expressed in terms of complex spherical eigenvectors:[39]

$$\mathbf{E}_{in} = \sum_{n=1}^{\infty} E_n \left[c_n^{(l)} \mathbf{M}_{o1n}^{(1)} - id_n^{(l)} \mathbf{N}_{e1n}^{(1)} \right] \quad (1)$$

$$\mathbf{E}_{out} = \sum_{n=1}^{\infty} E_n \left[ia_n^{(l)} \mathbf{N}_{e1n}^{(3)} - b_n^{(l)} \mathbf{M}_{o1n}^{(3)} \right] \quad (2)$$

where $E_n = i^n E_0 (2n + 1)/n(n + 1)$, $\mathbf{M}_{o1n}^{(j)}$ and $\mathbf{N}_{e1n}^{(j)}$ ($j = 1, 3$) are the vector spherical harmonics and the superscripts denote the kind of Bessel function (explicit expressions can be found elsewhere, for instance in the book by Bohren and Huffman[44]). Now, the electric and magnetic fields in each layer can be calculated by:

$$\mathbf{E}_l = \sum_{n=1}^{\infty} E_n \left[c_n^{(l)} \mathbf{M}_{o1n}^{(1)} - id_n^{(l)} \mathbf{N}_{e1n}^{(1)} + ia_n^{(l)} \mathbf{N}_{e1n}^{(3)} - b_n^{(l)} \mathbf{M}_{o1n}^{(3)} \right] \quad (3)$$

$$\mathbf{H}_l = \frac{k_l}{\omega\mu} \sum_{n=1}^{\infty} E_n \left[d_n^{(l)} \mathbf{M}_{e1n}^{(1)} + ic_n^{(l)} \mathbf{N}_{o1n}^{(1)} - ib_n^{(l)} \mathbf{N}_{o1n}^{(3)} - a_n^{(l)} \mathbf{M}_{e1n}^{(3)} \right] \quad (4)$$
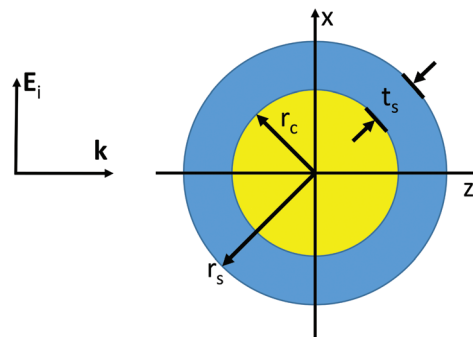

Fig. 1 Schematic representation of a core@shell NP. r_c and r_s are the core and shell radii, respectively, and t_s is the thickness of the shell.

where ω is the angular frequency of the incident wave and μ is the magnetic permeability of the l region. The expansion coefficients $a_n^{(l)}$, $b_n^{(l)}$, $c_n^{(l)}$ and $d_n^{(l)}$ are obtained by matching the tangential components of the electromagnetic fields at each interface.[44] Therefore, the expressions for expansion coefficients are:[45]

$$a_n^{(l)} = \frac{D_n^{(1)}(m_l x_l) T_1(m_{l+1} x_l) + T_3(m_{l+1} x_l) m_l / m_{l+1}}{\zeta_n(m_l x_l) \left(D_n^{(1)}(m_l x_l) - D_n^{(3)}(m_l x_l) \right)} \quad (5)$$

$$b_n^{(l)} = \frac{D_n^{(1)}(m_l x_l) T_2(m_{l+1} x_l) m_l / m_{l+1} + T_4(m_{l+1} x_l)}{\zeta_n(m_l x_l) \left(D_n^{(1)}(m_l x_l) - D_n^{(3)}(m_l x_l) \right)} \quad (6)$$

$$c_n^{(l)} = \frac{D_n^{(3)}(m_l x_l) T_2(m_{l+1} x_l) m_l / m_{l+1} + T_4(m_{l+1} x_l)}{\psi_n(m_l x_l) \left(D_n^{(1)}(m_l x_l) - D_n^{(3)}(m_l x_l) \right)} \quad (7)$$

$$d_n^{(l)} = \frac{D_n^{(3)}(m_l x_l) T_1(m_{l+1} x_l) + T_3(m_{l+1} x_l) m_l / m_{l+1}}{\psi_n(m_l x_l) \left(D_n^{(1)}(m_l x_l) - D_n^{(3)}(m_l x_l) \right)} \quad (8)$$

where

$$T_1(m_{l+1} x_l) = a_n^{(l+1)} \zeta_n(m_{l+1} x_l) - d_n^{(l+1)} \psi_n(m_{l+1} x_l) \quad (9)$$

$$T_2(m_{l+1} x_l) = b_n^{(l+1)} \zeta_n(m_{l+1} x_l) - c_n^{(l+1)} \psi_n(m_{l+1} x_l) \quad (10)$$

$$T_3(m_{l+1} x_l) = d_n^{(l+1)} D_n^{(1)}(m_{l+1} x_l) \psi_n(m_{l+1} x_l) - a_n^{(l+1)} D_n^{(3)}(m_{l+1} x_l) \zeta_n(m_{l+1} x_l) \quad (11)$$

$$T_4(m_{l+1} x_l) = b_n^{(l+1)} D_n^{(1)}(m_{l+1} x_l) \psi_n(m_{l+1} x_l) - c_n^{(l+1)} D_n^{(3)}(m_{l+1} x_l) \zeta_n(m_{l+1} x_l) \quad (12)$$

and $c_n^{(L+1)} = d_n^{(L+1)} = 1$ ($L + 1$ refers to the region outside the particle, where EM waves are strictly equal to the incident field), $a_n^{(L+1)} = a_n$, $b_n^{(L+1)} = b_n$ (a_n and b_n are the scattering coefficients), $D_n^{(1)} = \psi'_n / \psi_n$ and $D_n^{(3)} = \zeta'_n / \zeta_n$, where ψ_n and ζ_n are the Riccati–Bessel functions.

We have analysed the effects of alloy composition, core size, and shell thickness on near-field enhancements for bare and core–shell alloy NPs. The SERS enhancement factor of plasmonic nanostructures is proportional to the fourth power of the near-field enhancement ($|\mathbf{E}|^4 / |\mathbf{E}_0|^4$);[41] consequently, we have used this quantity to represent the field enhancement. Results are presented in terms of the maximum electric field, $\max(|\mathbf{E}|^4 / |\mathbf{E}_0|^4) = |\mathbf{E}_{\max}|^4 / |\mathbf{E}_0|^4$, around the surface of the alloy core and silica shell. Near-field was calculated 0.5 nm away from the surface (see the dotted circle in the inset of Fig. 2d) using an angular resolution of 0.5 degrees. The distance of 0.5 nm from the surface was used in order to avoid the instability of the electric field at the interface of two media, and taking into account the common interaction distance between the adsorbed analyte and the SERS substrate. Calculations were performed from 300 nm to 1000 nm, with a
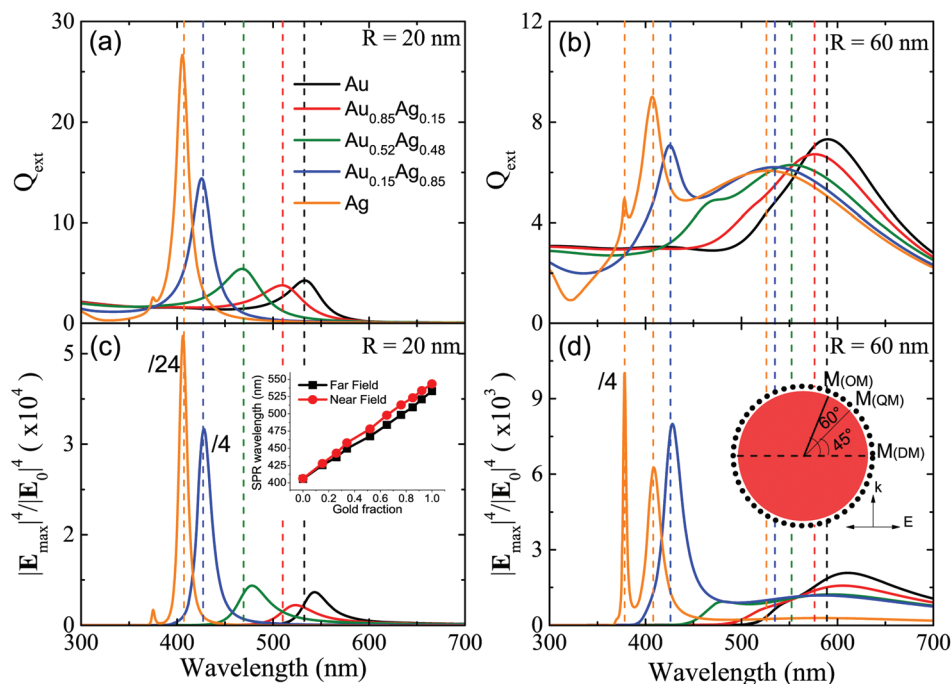

Fig. 2 (a, b) Extinction efficiency and (c, d) maximum near electric field enhancement spectra for the bare $Au_x Ag_{1-x}$ NPs of radius (a), (c) 20 nm and (b), (d) 60 nm with different compositions. The vertical dashed lines situated at the maximum of each SPR mode in Q_{ext} and extended to $|\mathbf{E}|^4 / |\mathbf{E}_0|^4$ plots are presented to appreciate the relative change of the SPR modes in the near field. Inset in (d) shows the position of SPR bands for spherical $Au_x Ag_{1-x}$ NPs. The inset in (c) represents the variation of the LSPR maximum in the far- (black squares) and the near-field (red circles) as a function of the gold fraction for 20 nm $Au_x Ag_{1-x}$ NPs.

resolution of 0.5 nm. Although the near-field (NF) and far-field (FF) optical properties of Au_xAg_{1-x} alloy cores with Au molar fractions x_{Au} = 1 (pure Au), 0.92, 0.85, 0.76, 0.65, 0.52, 0.34, 0.26, 0.15, and 0 (pure Ag) were calculated, only the results of representative compositions are presented.

Results and discussion

The extinction efficiency (Q_{ext}) and fourth-power of the near electric field ($|\mathbf{E}|^4/|\mathbf{E}_0|^4$) in the surroundings of a bare Au_xAg_{1-x} alloy nanoparticle are depicted in Fig. 2, for small (R = 20 nm) and large (R = 60 nm) structures, to compare the features of both properties. For the smaller particle (Fig. 2a and c), the intensity of the localized surface plasmon resonance, both in the FF and the NF, as a function of x_{Au} first decreases down to around the composition with 85% of gold, and then increases. Finally, the LSPR position shows a quasi-linear dependence on x_{Au} (inset of Fig. 2c). This linear dependence of the LSPR position on x_{Au} has also been observed experimentally by other authors.[33,46–49] To understand this effect, we must consider that gold and silver are quite similar in their electronic structures[50,51] so that it can be expected that the band structure as such will be preserved throughout the alloy system. On the other hand, the energy threshold for interband transitions between s- and d-bands is quite different, at ~2.4 eV and ~4.0 eV for gold and silver, respectively.[52] The electrons that constitute the surface plasmon (s-band electrons) can give their energy to promote electronic transitions, which considerably redshifts the LSPR.[46] The energy gap between the d-bands and the Fermi level is linearly reduced with the increase of the gold fraction, resulting in the observed linear dependence.

Two competing factors might be responsible for the aforementioned variations in intensity. Firstly, the bandgap reduction increases the interaction between the plasmon and the interband transitions of the alloy, producing a strong damping and broadening of the LSPR band and decreasing its intensity.[53,54] On the other hand, distortions of the metal lattice due to the presence of two types of metal atoms affect the electron mobility in alloy particles,[54,55] which in turn affects the oscillation of plasma electrons and produces a quadratic dependence of the damping constant.[38] Maximum damping occurs for nearly-equal concentrations of the component metals.[38,55] A combination of both effects can yield the observed changes in the intensity and width of the LSPR with the shift of maximum damping for higher gold concentrations. This nonlinear dependence of the LSPR intensity on x_{Au} agrees well with the reported experimental results,[46] with certain deviation due to the size dispersion and/or uncertainty in the determination of the alloy composition experimentally.

For the larger particle (Fig. 2b and d), the situation is further complicated by the damping of the LSPR due to size effects (red-shift of the LSPR, and production of higher order modes) but the main mechanisms are essentially the same. It should be noted that in all cases the nonlinearity of the damping constant, Γ, relative to x_{Au} does not significantly

influence the LSPR position as the real and imaginary parts of the complex dielectric function ($\varepsilon = \varepsilon' + i\varepsilon''$) in the Drude mode, defined as $\varepsilon' = \varepsilon_\infty - \omega_p^2/(\omega^2 + \Gamma^2)$ and $\varepsilon'' = \omega_p^2\Gamma/\omega(\omega^2 + \Gamma^2)$, are almost independent of Γ around the LSPR frequency ($\omega \gg \Gamma$).[44]

The maxima of the different multipolar modes depicted in Fig. 2 are not in the same geometrical position. The maximum of the dipolar mode is located in the X axis (i.e., parallel to the polarization of the incident wave) but the same is not true for the quadrupolar and octupolar modes, whose maxima are located at 45° and 60° with respect to the X axis, respectively, as depicted in the inset of Fig. 2d. From the $|\mathbf{E}|^4/|\mathbf{E}_0|^4$ spectra plotted just below the corresponding extinction spectra (Fig. 2c and d), it can be seen that the maximum near-field enhancement is located at a longer wavelength with respect to that of the extinction efficiency (i.e., the far-field).

Furthermore, the relative intensities of different multipolar modes are quite different in the NF compared to the FF. Let's take as an example a 60 nm $Au_{0.15}Ag_{0.85}$ NP (blue lines, Fig. 2b and d). The intensity of its quadrupolar mode in the NF is almost twice (16 times for the fourth power) that of the dipolar mode (Fig. 2d); whereas they are very similar in the FF (Fig. 2b). This behaviour can be explained by considering the variation in the electric field decay rates: for higher modes the reduction of the electric field with the distance (r) from the particle's centre is larger. For example, the electric field decay is proportional to r^{-3} for the dipolar mode, r^{-4} for the quadru-
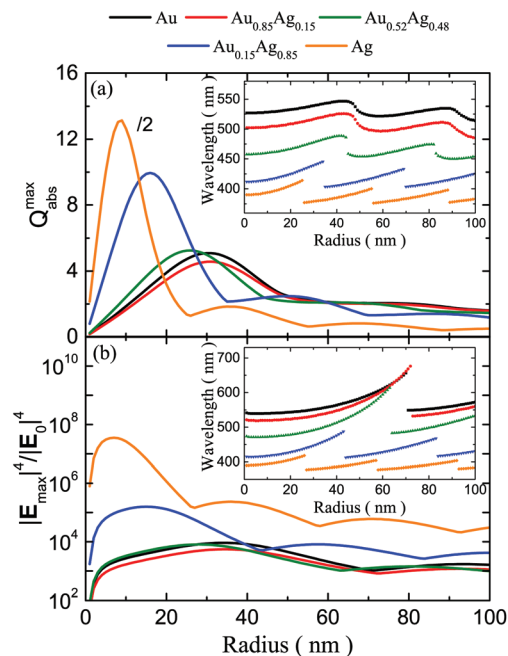

Fig. 3 Variation of (a) absorption efficiency and (b) near electric field (computed at a distance of 0.5 nm from the NP surface) with the size of Au_xAg_{1-x} NPs. The compositions of the bimetallic NPs are indicated in (a). The insets are the plots of wavelengths corresponding to the maximum value of the absorption efficiency and the near electric field as a function of the nanoparticle radius, respectively.
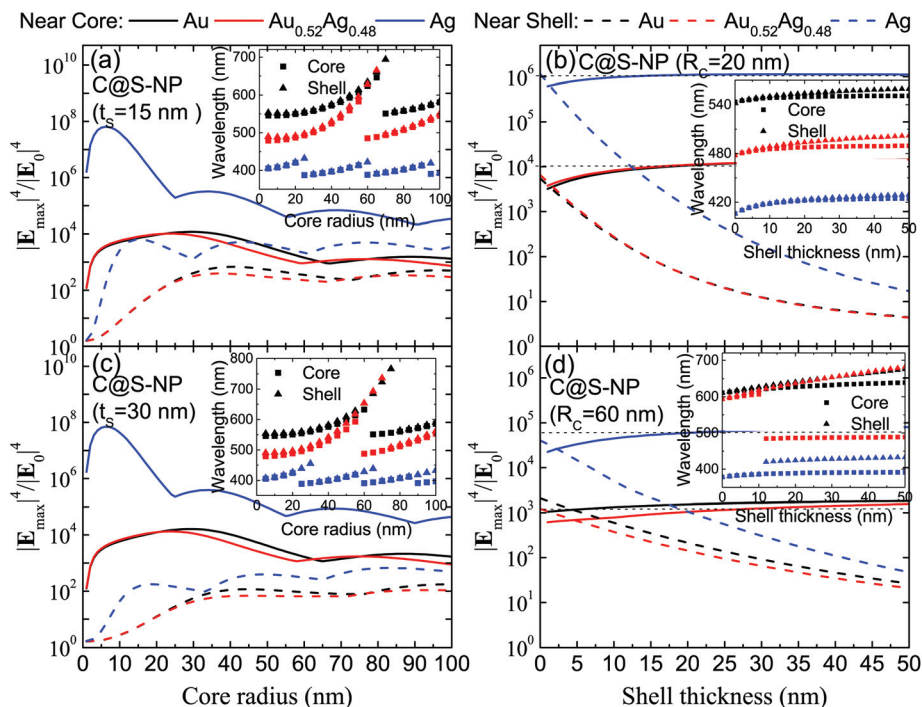
Fig. 4 Maximum value of the fourth-power of the near electric field, computed at a distance of 0.5 nm away from the core surface (solid lines) and from the shell surface (dashed lines) as a function of the core radius for the fixed shell thickness (a) 15 nm and (c) 30 nm, and as a function of shell thickness for the fixed core radius of (b) 20 nm and (d) 60 nm. Core particles of three compositions have been considered for all the plots. The insets are the plots of the wavelengths corresponding to the maximum value of the near electric field around the core (squares) and the shell (triangles) as a function of the nanoparticle radius and shell thickness, respectively.

polar and so on. Therefore, precautions must be taken when selecting plasmonic NPs for use in NF applications based on results obtained from measurements and/or calculations in the FF. In these cases, it is always advisable to make NF calculations to determine the intensity, width, and position of the LSPR modes because these properties might be different in the NF with respect to those of the FF.

The maximum absorption efficiency (Q_{abs}^{max}) and field enhancement $|E_{max}|^4/|E_0|^4$ around Au_xAg_{1-x} NPs are plotted against the NP radius (from 1 to 100 nm) in Fig. 3a and b, respectively. Each step observed in the "leapfrog" behaviour in the intensity of both Q_{abs} and $|E_{max}|^4/|E_0|^4$ is related with a change in the dominant multipolar mode, and the discontinuities in the plots of LSPR wavelength *vs.* radius (insets of Fig. 3a and b) come from the changes in the relative intensity of different modes. Both quantities, Q_{abs}^{max} and $|E_{max}|^4/|E_0|^4$ follow similar trends, with a global maximum corresponding to the dipolar mode for a specific radius. This radius increases proportionally to the gold fraction in the alloy particles, which also increases the offset between the maxima of the Q_{abs} and $|E|^4/|E_0|^4$ peaks. As can be seen from the plots of LSPR position *versus* radius (insets of Fig. 3a and b), the maximum of the Q_{abs} peak gets marginally red-shifted with increasing NP radius whereas the red-shift of $|E_{max}|^4/|E_0|^4$ is substantial (the scattering efficiency, not shown, is also considerably shifted).
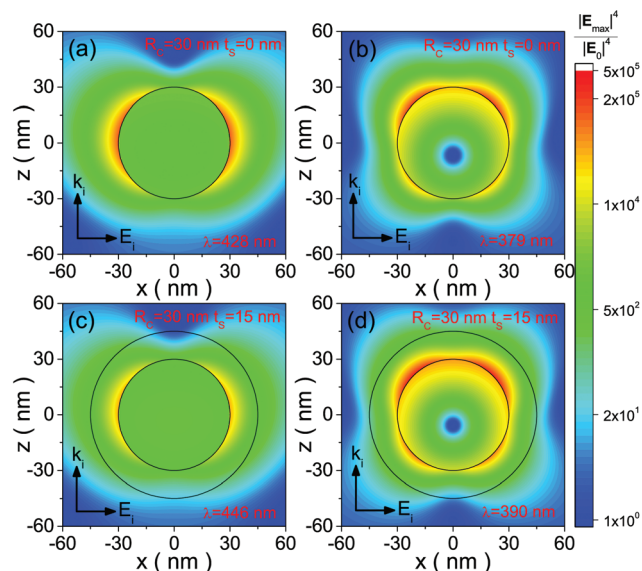

Fig. 5 Near electric field distribution maps for (a, b) a bare silver nanoparticle of 30 nm radius, (c, d) an Ag@SiO₂ NP of 30 nm core radius and 15 nm shell thickness. The left column contains maps computed at the maximum dipolar LSPR and the right one for the maximum quadrupolar LSPR.

For example, the position of Q_{abs}^{max} for Au NPs shifts from 520 nm to 550 nm with the increase of particle radius, whereas $|E_{max}|^4/|E_0|^4$ shifts from 540 to 660 nm. This is because both $|E_{max}|^4/|E_0|^4$ and the scattering efficiency are strongly dependent on the damping constant, which increases with the NP radius due to the retardation effect of the depolarization field[3] and also with the distortion of the metal lattice of the alloy NPs. Ag-rich NPs have very similar shifts for Q_{abs}^{max} and $|E_{max}|^4/|E_0|^4$, probably due to the weak dependence of the latter quantity on Γ.

The variation of field enhancement $|E_{max}|^4/|E_0|^4$ around the core (solid line) and around the shell (dashed line) with the radius of the core particle (R_C, from 1 to 100 nm) for two shell thicknesses ($t_s = 15$ nm and 30 nm) of the alloy-core@SiO$_2$-shell NPs are presented in Fig. 4. It can be seen that for some core radii the maximum electric fields around the shell and the core have contributions of modes of different orders. For example, the maximum electric field near the core of the Ag@SiO$_2$ NP with $R_C = 30$ nm and $t_s = 30$ nm is due to the quadrupolar mode, but the maximum near the shell for the same NP comes from the dipolar mode (Fig. 4c and its inset). This is the consequence of the different relationships of the field intensity with the propagation distance for each mode (as previously discussed); *i.e.*, a multipolar mode can be more
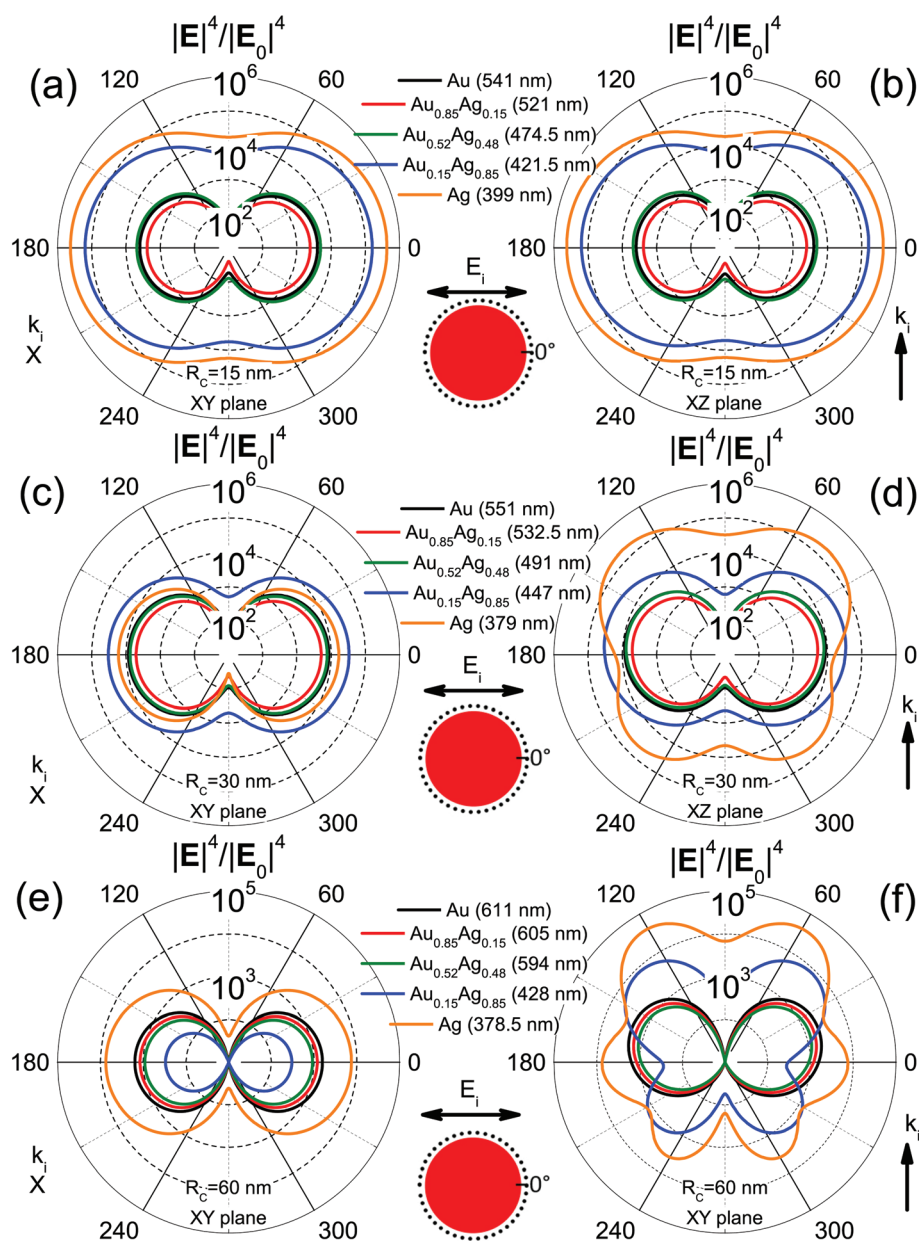

Fig. 6 Polar plots of the near electric field distribution around a bare nanoparticle (computed at a distance of 0.5 nm from its surface) of (a, b) 15 nm, (c, d) 30 nm, and (e, f) 60 nm radius. The left column is for the *XY* plane and the right one is for the *XZ* plane. The analysed compositions (Au$_x$Ag$_{1-x}$) and the wavelength of the maximum $|E_{max}|^4/|E_0|^4$ are indicated in the figure.

intense than a lower order mode close to the core whereas the opposite can be true for the shell. Moreover, it can be seen in Fig. 4a and c that regardless of the alloy composition, the maximum enhancement around the core decreases with increasing core radius; but the opposite is true for the maximum enhancement around the shell. It can be noted that the $|\mathbf{E}_{max}|^4/|\mathbf{E}_0|^4$ near the shell of an Ag@SiO$_2$ NP with $R_C > 50$ and $t_s = 15$ nm is more intense than that of a core–shell NP with the same geometry but with a metal alloy core ($x_{Au} = 0.52$).

To better understand the effects of the silica shell on the optical properties of Au$_x$Ag$_{1-x}$ alloy NPs, $|\mathbf{E}_{max}|^4/|\mathbf{E}_0|^4$ is plotted against the shell thickness ($t_s = 0$ to 50 nm) for a small ($R_C = 20$ nm) and a large ($R_C = 60$ nm) particle in Fig. 4b and d, respectively. Compared to the case of bare NPs, the electric field near the surface of the core of a core–shell NP with a thin shell remains essentially the same, except that it is less intense. However, we can see from Fig. 4b and d that the electric field close to the core increases asymptotically up to a
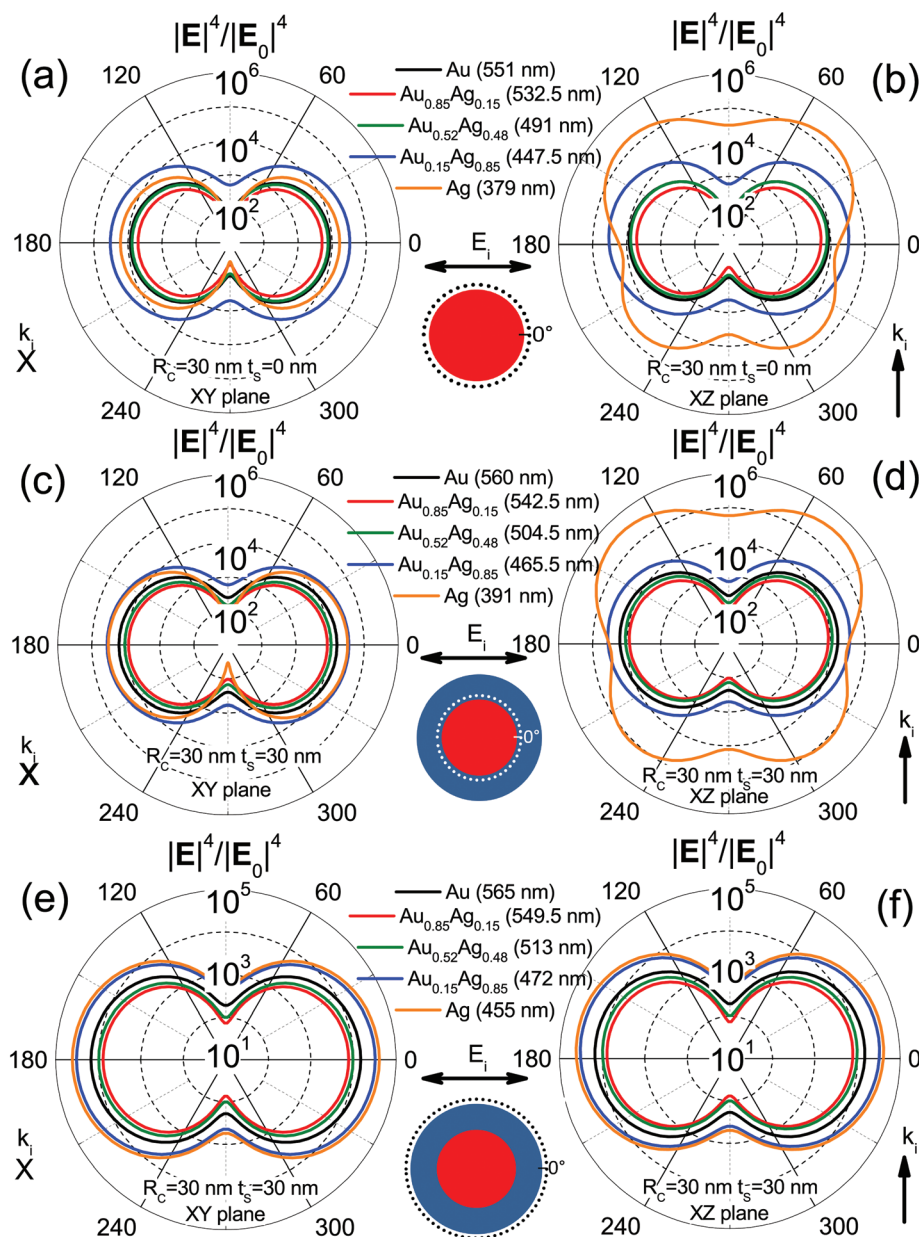

Fig. 7 Polar plots of the near electric field distribution (at LSPR wavelength) around (a, b) a bare nanoparticle of 30 nm radius, (c, d) near the core of a core@SiO$_2$ NP of 30 nm core radius and 30 nm shell thickness, and (e, f) near the shell of the same NP as (c, d). The fields are computed at a distance of 0.5 nm from the corresponding surface (dashed circumferences on the schemes between plots indicate where was the electric field measured). Left column is for the *XY* plane and the right one is for the *XZ* plane. The analysed compositions of the Au$_x$Ag$_{1-x}$ NPs are indicated in the figure.

constant value (black dashed lines) with increasing shell thickness. Close to the core the electric field is slightly more intense for the NP with a thicker silica shell than for a bare NP with similar dimensions, due to the increase of the dielectric function around the core. The near electric field intensity at the shell surface decreases with shell thickness due to the increase of distance from the core. However, the position of the electric field maximum varies only marginally with shell thickness (insets of Fig. 4b and d). The energy difference (wavelength shift) between the electric field maxima of the core and the shell varies for different compositions of the core. While for a core with a high silver content the difference is virtually zero, the difference is maximal for the core with compositions close to $Au_{0.5}Ag_{0.5}$. In addition, the modes exhibiting the maximum field enhancement can be swapped as the shell thickness increases, which is illustrated in the discontinuities observed in the inset of Fig. 4d. For instance, the maximum field near the core of an $Au_{0.52}Ag_{0.48}@SiO_2$ NP corresponds to a dipolar mode (R_c = 60 nm, t_s < 10 nm) but changes to quadrupolar for thicker shells (t_s > 10 nm).

Near electric field distribution maps are shown in Fig. 5 for a bare silver NP (R_c = 30 nm; t_s = 0 nm) and a core–shell structure (R_c = 30 nm; t_s = 15 nm). In the former case the near-field spectrum has two maxima, the larger one (the quadrupolar mode) is located at 379 nm (Fig. 5b), whereas the smaller (the dipolar mode) is located around 428 nm (Fig. 5a), the latter being three times less intense than the former. When the bare nanoparticle is capped with a dielectric shell, the electric field enhancement near the core associated with the dipolar mode decreases from 6.4×10^4 to 5×10^4 (21%, Fig. 5c), and it suffers a red-shift with the new maximum located at 446 nm. However, the field associated with the quadrupolar mode enhances from 2×10^5 to 3.5×10^5 (75%), suffering a red-shift to 390 nm (Fig. 5d). The electric field enhancement decays rapidly by several orders of magnitude just a few nanometres away from the core, indicating that the analyte molecules must reside very close to the core surface in order to obtain the maximum response in SERS applications.

The distribution of the oscillating conduction electrons inside a metal NP is more homogeneous when it is excited at the dipolar-mode wavelength (Fig. 5a and c) rather than at the quadrupolar-mode wavelength (Fig. 5b and d), because the electrons oscillate away from the centre for the latter case. The same is true for all the higher-order modes. The asymmetry of spatial distribution of the electric field in the plane of incidence is due to the opposite direction of the entrance of the field lines (into the NP) with respect to the direction of excitation light.[56]

Polar plots of the maximum field enhancement around the surface of bare Au_xAg_{1-x} NPs are depicted in Fig. 6 (left and right columns represent the XY and XZ planes, respectively). It can be seen that for a small nanoparticle (Fig. 6a and b, R = 15 nm) the maximum field enhancement is predominantly dipolar and that for alloy NPs with high silver contents (Ag > 50%) the field enhancements are about two orders of magnitude larger than for the alloy NPs with higher Au contents. For

the silver NPs with larger radius (e.g. 30 nm, Fig. 6c and d), the intensity of the quadrupolar mode is much higher than the maximum of the dipolar mode (not presented), and it is no longer symmetric around the X axis in the XZ plane as in the case of smaller particles (Fig. 6b). The origin of this asymmetry is the same as described in the previous paragraph. A further increase of nanoparticle size to 60 nm induces the appearance of higher order modes with lower intensities, which are also asymmetric around the X axis in the XZ plane (Fig. 6e and f).

The effect of the shell over the field distribution around alloy NPs is analysed in Fig. 7. Field enhancement polar plots are nearly identical for a bare NP (Fig. 7a and b; R = 30 nm) and for a core–shell structure (Fig. 7c and d; R_c = 30 nm, t_s = 30 nm); the LSPR being predominantly quadrupolar for the silver core and dipolar for all the other alloy cores. The only appreciable effect of the shell is a slight increase of the electric field. Finally, the maximum of electric field enhancement around the shell (Fig. 7e and f) is dipolar in all cases because the quadrupolar mode is suppressed by damping with the propagation distance. From Fig. 6 and 7, we can see that the maxima of the dipolar mode are localized along the polarization direction whereas the maxima of the quadrupolar mode are located roughly at every 90° starting from 45° with respect to the polarization direction, and the maxima of the octupolar mode are located at every 60° from the polarization direction.

The appearance of predominant modes at the core and at the shell of core–shell NPs (shown in Fig. 7d and f for $Ag@SiO_2$ NPs) can be better appreciated in Fig. 8, where the maximum enhancements of the electric field near the core
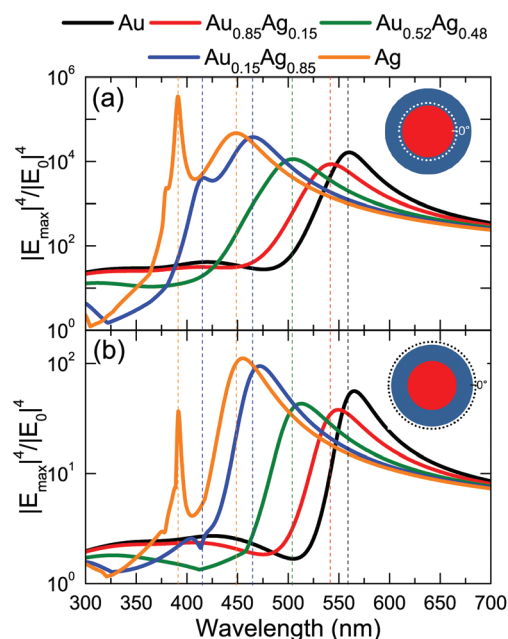

Fig. 8 Spectra of the near electric field maximum for $Au_xAg_{1-x}@SiO_2$ nanoparticles of 30 nm core radius and 30 nm shell thickness around (a) the core surface, and (b) at the shell surface, for different compositions of the Au_xAg_{1-x} core. The fields are computed at a distance of 0.5 nm from the corresponding surface (see insets).

(Fig. 8a) and the shell (Fig. 8b) are plotted as a function of wavelength. It can be clearly seen that the quadrupolar mode is dominant near the silver core (around 390 nm) but the dipolar mode is more intense in the surroundings of the shell. The quadrupolar mode almost disappears at the shell for the other compositions of the alloy core, causing the red-shift of the dipolar mode at the shell surface with respect to its position at the core surface (vertical dashed lines in Fig. 8) due to a lower contribution of the quadrupolar mode. Finally, there is an important enhancement of the near electric field for all the sizes of the NPs in the long wavelength region (Fig. 8), irrespective of their composition. This effect is a non-resonant contribution to the field enhancement in the quasi-static electric field regime, which depends on the curvature of the NP surface as the electric field lines concentrate near a surface with a high curvature.[57,58]

Conclusions

We have determined the near field enhancement around Au_xAg_{1-x} and $Au_xAg_{1-x}@SiO_2$ NPs using reliable optical parameters and the computer code scattnlay 2.0. Our calculations provide a detailed view of the intensity distribution around plasmonic NPs with different configurations, useful for optimizing these structures for near-field applications (like SERS, DSSCs and emission enhancements in OLEDs), where the interactions with analyte molecules occur close to the NPs' surface. The chemical instability of silver NPs limits their applications, a problem that is often overcome by alloying them with a small amount of gold. However, our results demonstrate that this solution is far from optimal because the field enhancement around Au_xAg_{1-x} NPs is lower than that of pure Ag NPs, depending on the gold fraction. This field enhancement is still high enough (between 10^4 and 10^8) for utilizing them as SERS substrates. Probably the best application of these alloy particles would be for enhancing the light emission in OLED devices, due to their tuneable LSPR. Finally, the red-shift of the LSPR is more pronounced in the near-field than in the far-field, which means that it is not possible to infer the LSPR trends in the near-field from those in the far-field. Hence, precise near-field experiments and calculations are necessary for designing optimum plasmonic structures for near-field applications like SERS, DSSCs and plasmon-enhanced OLEDs.

Acknowledgements

Notes and references

1 M.-C. Daniel and D. Astruc, *Chem. Rev.*, 2004, **104**, 293–346.
2 N. G. Bastús, J. Piella and V. Puntes, *Langmuir*, 2016, **32**, 290–300.
3 B. M. Ross and L. P. Lee, *Opt. Lett.*, 2009, **34**, 896.
4 S. S. R. Dasary, A. K. Singh, D. Senapati, H. Yu and P. C. Ray, *J. Am. Chem. Soc.*, 2009, **131**, 13806–13812.
5 D. Radziuk and H. Moehwald, *Phys. Chem. Chem. Phys.*, 2015, **17**, 21072–21093.
6 S. Kühn, U. Håkanson, L. Rogobete and V. Sandoghdar, *Phys. Rev. Lett.*, 2006, **97**, 17402.
7 W. Z. Liu, H. Y. Xu, C. L. Wang, L. X. Zhang, C. Zhang, S. Y. Sun, J. G. Ma, X. T. Zhang, J. N. Wang and Y. C. Liu, *Nanoscale*, 2013, **5**, 8634–8639.
8 C. Zhang, C. E. Marvinney, H. Y. Xu, W. Z. Liu, C. L. Wang, L. X. Zhang, J. N. Wang, J. G. Ma and Y. C. Liu, *Nanoscale*, 2014, **7**, 1073–1080.
9 G. L. Liu, Y.-T. Long, Y. Choi, T. Kang and L. P. Lee, *Nat. Methods*, 2007, **4**, 1015–1017.
10 K. Saha, S. S. Agasti, C. Kim, X. Li and V. M. Rotello, *Chem. Rev.*, 2012, **112**, 2739–2779.
11 K.-S. Lee and M. A. El-Sayed, *J. Phys. Chem. B*, 2006, **110**, 19220–19225.
12 P. K. Jain, X. Huang, I. H. El-Sayed and M. A. El-Sayed, *Acc. Chem. Res.*, 2008, **41**, 1578–1586.
13 M. D. Brown, T. Suteewong, R. S. S. Kumar, V. D'Innocenzo, A. Petrozza, M. M. Lee, U. Wiesner and H. J. Snaith, *Nano Lett.*, 2011, **11**, 438–445.
14 T. L. Temple, G. D. K. Mahanama, H. S. Reehal and D. M. Bagnall, *Sol. Energy Mater. Sol. Cells*, 2009, **93**, 1978–1985.
15 H. Choi, S.-J. Ko, Y. Choi, P. Joo, T. Kim, B. R. Lee, J.-W. Jung, H. J. Choi, M. Cha, J.-R. Jeong, I.-W. Hwang, M. H. Song, B.-S. Kim and J. Y. Kim, *Nat. Photonics*, 2013, **7**, 732–738.
16 M. Choe, C.-Y. Cho, J.-P. Shim, W. Park, S. K. Lim, W.-K. Hong, B. H. Lee, D.-S. Lee, S.-J. Park and T. Lee, *Appl. Phys. Lett.*, 2012, **101**, 31115.
17 S. D. Standridge, G. C. Schatz and J. T. Hupp, *J. Am. Chem. Soc.*, 2009, **131**, 8407–8409.
18 W. Wang, Z. Li, B. Gu, Z. Zhang and H. Xu, *ACS Nano*, 2009, **3**, 3493–3496.
19 R. Ghosh Chaudhuri and S. Paria, *Chem. Rev.*, 2012, **112**, 2373–2433.
20 H. Baida, P. Billaud, S. Marhaba, D. Christofilos, E. Cottancin, A. Crut, J. Lermé, P. Maioli, M. Pellarin, M. Broyer, N. Del Fatti, F. Vallée, A. Sánchez-Iglesias, I. Pastoriza-Santos and L. M. Liz-Marzán, *Nano Lett.*, 2009, **9**, 3463–3469.
21 K. Aslan, M. Wu, J. R. Lakowicz and C. D. Geddes, *J. Am. Chem. Soc.*, 2007, **129**, 1524–1525.
22 M. Lessard-Viger, M. Rioux, L. Rainville and D. Boudreau, *Nano Lett.*, 2009, **9**, 3066–3071.
23 P. Yang, K. Kawasaki, M. Ando and N. Murase, *J. Nanopart. Res.*, 2012, **14**, 1–11.

24 C. W. Tang and S. A. VanSlyke, *Appl. Phys. Lett.*, 1987, **51**, 913–915.

25 C. Adachi, M. A. Baldo, M. E. Thompson and S. R. Forrest, *J. Appl. Phys.*, 2001, **90**, 5048–5051.

26 C. F. Madigan, M.-H. Lu and J. C. Sturm, *Appl. Phys. Lett.*, 2000, **76**, 1650–1652.

27 S. Khadi, M. Chakaroun, A. Belkhi, A. Fische, O. Lamrous and A. Boudrioua, *Opt. Express*, 2015, **23**, 23647.

28 S.-H. Jeong, H. Choi, J. Y. Kim and T.-W. Lee, *Part. Part. Syst. Charact.*, 2015, **32**, 164–175.

29 Y. H. Lee, D. H. Kim, K.-H. Yoo and T. W. Kim, *Appl. Phys. Lett.*, 2014, **105**, 183303.

30 W. Wang, X. Shi, N. N. Kariuki, M. Schadt, G. R. Wang, Q. Rendeng, J. Choi, J. Luo, S. Lu and C.-J. Zhong, *J. Am. Chem. Soc.*, 2007, **129**, 2161–2170.

31 V. K. Rao and T. P. Radhakrishnan, *ACS Appl. Mater. Interfaces*, 2015, **7**, 12767–12773.

32 X. Liu, A. Wang, X. Yang, T. Zhang, C.-Y. Mou, D.-S. Su and J. Li, *Chem. Mater.*, 2009, **21**, 410–418.

33 C. Wang, H. Yin, R. Chan, S. Peng, S. Dai and S. Sun, *Chem. Mater.*, 2009, **21**, 433–435.

34 S. W. Verbruggen, M. Keulemans, M. Filippousi, D. Flahaut, G. Van Tendeloo, S. Lacombe, J. A. Martens and S. Lenaerts, *Appl. Catal., B*, 2014, **156–157**, 116–121.

35 N. Li, X. Zhang, S. Yuan, X. Zhang, Y. Yuan and X. Li, *Phys. Chem. Chem. Phys.*, 2015, **17**, 12023–12030.

36 M. Xu, J. Feng, Y.-S. Liu, Y. Jin, H.-Y. Wang and H.-B. Sun, *Appl. Phys. Lett.*, 2014, **105**, 153303.

37 W. Cui, M. Li, Z. Dai, Q. Meng and Y. Zhu, *J. Chem. Phys.*, 2014, **140**, 44109.

38 O. Peña-Rodríguez, M. Caro, A. Rivera, J. Olivares, J. M. Perlado and A. Caro, *Opt. Mater. Express*, 2014, **4**, 403–410.

39 O. Peña and U. Pal, *Comput. Phys. Commun.*, 2009, **180**, 2348–2354.

40 G. Mie, *Ann. Phys.*, 1908, **330**, 377–445.

41 *Surface-enhanced Raman scattering*, ed. K. Kneipp, M. Moskovits and H. Kneipp, Springer, Berlin, Heidelberg, 2006, vol. 103.

42 L. Gao, F. Lemarchand and M. Lequime, *J. Eur. Opt. Soc. Rapid Publ.*, 2013, **8**, 13010.

43 I. Thormählen, J. Straub and U. Grigull, *J. Phys. Chem. Ref. Data*, 1985, **14**, 933–945.

44 C. F. Bohren and D. R. Huffman, *Absorption and scattering of light by small particles*, Wiley-Interscience, 1998.

45 W. Yang, *Appl. Opt.*, 2003, **42**, 1710–1720.

46 S. Link, Z. L. Wang and M. A. El-Sayed, *J. Phys. Chem. B*, 1999, **103**, 3529–3533.

47 J. F. Sánchez-Ramírez, U. Pal, L. Nolasco-Hernández, J. Mendoza-Álvarez, J. A. Pescador-Rojas, J. F. Sánchez-Ramírez, U. Pal, L. Nolasco-Hernández, J. Mendoza-Álvarez and J. A. Pescador-Rojas, *J. Nanomater.*, 2008, **2008**, 620412.

48 G. C. Papavassiliou, *J. Phys. F: Met. Phys.*, 1976, **6**, L103.

49 S. Liu, G. Chen, P. N. Prasad and M. T. Swihart, *Chem. Mater.*, 2011, **23**, 4098–4101.

50 N. E. Christensen and B. O. Seraphin, *Phys. Rev. B: Solid State*, 1971, **4**, 3321–3344.

51 N. E. Christensen, *Phys. Status Solidi B*, 1972, **54**, 551–563.

52 E. Cottancin, G. Celep, J. Lermé, M. Pellarin, J. R. Huntzinger, J. L. Vialle and M. Broyer, *Theor. Chem. Acc.*, 2006, **116**, 514–523.

53 O. Peña, U. Pal, L. Rodríguez-Fernández and A. Crespo-Sosa, *J. Opt. Soc. Am. B*, 2008, **25**, 1371–1379.

54 Z. Pirzadeh, T. Pakizeh, V. Miljkovic, C. Langhammer and A. Dmitriev, *ACS Photonics*, 2014, **1**, 158–162.

55 Y. Nishijima and S. Akiyama, *Opt. Mater. Express*, 2012, **2**, 1226–1235.

56 M. Bashevoy, V. Fedotov and N. Zheludev, *Opt. Express*, 2005, **13**, 8372–8379.

57 N. K. Grady, N. J. Halas and P. Nordlander, *Chem. Phys. Lett.*, 2004, **399**, 167–171.

58 S. Raza, S. Kadkhodazadeh, T. Christensen, M. Di Vece, M. Wubs, N. A. Mortensen and N. Stenger, *Nat. Commun.*, 2015, **6**, 8788.